J Mater Sci: Mater Electron
DOI 10.1007/s10854-012-0768-8

Role of annealing temperature on microstructural and electro-optical properties of ITO films produced by sputtering

M. Gulen · G. Yildirim · S. Bal · A. Varilci · I. Belenli · M. Oz

Received: 21 March 2012 / Accepted: 18 May 2012

Abstract This study probes the effect of annealing temperature on electrical, optical and microstructural properties of indium tin oxide (ITO) films deposited onto soda lime glass substrates by conventional direct current (DC) magnetron reactive sputtering technique at 100 watt using an ITO ceramic target (In_2O_3:SnO_2, 90:10 wt%) in argon atmosphere at room temperature. The films obtained are exposed to the calcination process at different temperature up to 700 °C. X–ray diffractometer (XRD), ultra violet-visible spectrometer (UV–vis) and atomic force microscopy (AFM) measurements are performed to characterize the samples. Moreover, phase purity, surface morphology, optical and photocatalytic properties of the films are compared with each other. The results obtained show that all the properties depend strongly on the annealing temperature. XRD results indicate that all the samples produced contain the In_2O_3 phase only and exhibit the polycrystalline and cubic bixbite structure with more intensity of diffraction lines with increasing the annealing temperature until 400 °C; in fact the strongest intensity of (*222*) peak is obtained for the sample annealed at 400 °C, meaning that the sample has the greatest ratio I_{222}/I_{400} and the maximum grain size (54 nm). As for the AFM results, the sample prepared at 400 °C has the best microstructure with the lower surface roughness. Additionally, the transmittance measurements illustrate that the amplitude of interference oscillation is in the range from 78 (for the film annealed at 400 °C) to 93 % (for the film annealed at 100 °C). The refractive index, packing density, porosity and optical band gap of the ITO thin films are also evaluated from the transmittance spectra. According to the results, the film annealed at 400 °C obtains the better optical properties due to the high refractive index while the film produced at 100 °C exhibits much better photoactivity than the other films as a result of the large optical energy band gap.

1 Introduction

Since the discovery of the transparent conducting oxide (TCO) films, researchers have endeavored to improve their electrical, optical and microstructural properties to make them suitable for the advanced technological devices such as solar cells, light emitting diodes, photodiodes, photocatalysts, optical memories, flat panel displays, gas sensors, energy efficient windows, storage-type cathode ray tubes, surface layers in electroluminescent applications [1–9]. Indium tin oxide (ITO) films are the most promising materials for the potential technological and industrial applications including solar cell, liquid crystal displays and photodetectors, etc. [10–13] because of the higher optical transparency, lower resistivity, chemical stability, excellent adhesion and etching properties compared to other transparent and conducting oxide films such as TiO_2, SnO_2 or ZnO [14–18]. As well known, the ITO material behaves as an insulator in its stoichiometric form while the material is a conductor in the non-stoichiometric form with a wide direct optical band gap of 3.6 eV [19], resulting from the formation of a conducting carrier-oxygen vacancies with the addition of a dopant tetravalent cation Sn^{+4} to the matrix In_2O_3. Thus, the oxygen vacancies acting as doubly-

M. Gulen (✉) · G. Yildirim · S. Bal · A. Varilci · I. Belenli
Department of Physics, Abant Izzet Baysal University, 14280 Bolu, Turkey
e-mail: mahirglen@gmail.com

M. Oz
Department of Chemistry, Abant Izzet Baysal University, 14280 Bolu, Turkey

Published online: 29 May 2012

ionized donors contribute maximum two electrons to the electrical conductivity in the sample [20]. As a result, the conductivity of the ITO sample changes. The preparation conditions such as the operational procedures, annealing ambient (time, temperature atmosphere and pressure), composition, type and quantity of the dopant and heat-treatment method also affect the level of the conducting carrier concentration and oxygen vacancies. In particular, the annealing ambient plays a very significant role on the fabrication of the high-quality ITO films. It is argued that the crystallinity of the ITO thin films improves with the post-deposition annealing temperature because of the decrement in the structural defects [21–24]. In other words, the variation of the optical and electrical characteristics for the ITO thin film studied stems from the changes in the local ordering of the material during crystallization and the oxygen vacancy creation [16]. In order to prepare high quality ITO film, several deposition techniques such as thermal evaporation, chemical vapor deposition, electron beam evaporation, sol–gel, spray pyrolysis, pulsed laser deposition and magnetron sputtering have been experienced for years [25–29]. The conventional sputtering methods, among others, are the most preferred technique due to the reproducible deposition of the films accomplished quite easily compared to the other methods [30].

In the current study, the effect of the various annealing temperature on the microstructural, optical and electronical properties of the ITO thin films produced via DC sputtering method is examined by means of the X–ray diffractometer (XRD), atomic force microscopy (AFM) and ultra violet-visible spectrometer (UV–vis) measurements. Optical energy band gaps, porosities, packing densities and refraction indices deduced from transmittance spectra are also discussed clearly.

2 Experimental details

Deposition of the ITO thin films on soda lime glasses is conducted by DC magnetron sputtering system (NSC–3000 DC Sputter Machine) using an oxide ceramic target composed of 90 wt% In_2O_3 and 10 wt% SnO_2. Prior to the film deposition process, all the substrates are ultrasonically cleaned by acetone, degreased in a dilute detergent solution, rinsed thoroughly with deionized water and blown dry in nitrogen flow. ITO disk (99.99 % pure) with a 50 mm in diameter and a 4 mm in thickness is used as sputtering target. The substrates are vertically placed onto the substrate holder and the distance between them is adjusted to be about 60 mm. The chamber is evacuated down to a pressure lower than 10^{-6} Torr and the sputtering process is performed in 99.999 % pure argon (30 sscm for sputtering gas) at a DC power of 100 W. During the deposition, the substrates are kept at room temperature for 10 min. The ITO films removed from the sputtering system are exposed to the calcination process at different temperature in a range of 100–700 °C for 2 h in the tube furnace (Protherm-Model PTF12/75/200). The ITO films will be herein after denoted as ITO-100, ITO-200, ITO-300, ITO-400, ITO-500, ITO-600 and ITO-700, respectively.

The crystallographic structures of the ITO films studied are examined via X-ray diffraction (XRD) method by using the nickel-filtered Kα emission line ($\lambda = 1.5418$ Å) of copper in the range $2\theta = 20$–$60°$ at a scan speed of 3°/min and a step increment of 0.02° at room temperature in a Rigaku Multiflex instrument. The measurements are carried out under beam acceleration conditions of 38 kV/28 mA. Average crystallite sizes of the samples are derived from the Scherrer–Warren approach with the aid of the broadening nature of the XRD peaks when interplaner distance and lattice constant values are deduced from the peak (*222*). At the same time, optical measurements of the films obtained are performed by the unpolarized light at normal incidence in the wavelength range of 400–700 nm, with a JASCO 430 UV–VIS spectrophotometer. Refractive index (n_λ), porosity and optical band gap energy values of the films are calculated with the help of the transmittance spectra. Further, morphological features of ITO thin films prepared are examined using AFM (Nanomagnetic Instrument). Topographic and phase images are obtained in the non-contact mode under room conditions with typical rate of about 1 line per second with a resonance frequency of about 300 kHz. Measurements are performed with 512 scan lines. Several regions on the specimen surface are scanned to observe the similar images. AFM images analysis is carried out with special software written by Nanomagnetic Instrument group. Analysis is performed in the non-contact mode. Moreover, the AFM measurements are conducted with an imaging aspect ratio of 1:4 to minimize the signal distortion in the scan slow direction due to thermal drift [31–33]. Height asymmetries for the films are also discussed clearly.

3 Results and discussion

3.1 X–ray diffraction patterns

The X-ray diffraction patterns between 20° and 60° for the ITO films grown on the glass substrates at different annealing temperatures are shown in Fig. 1. The diffraction patterns obtained are used to determine the texture, grain size, interplaner distance and lattice constant parameters of the thin films. The deposition conditions of all the samples except for the post annealing temperature are kept constant during the film fabrication process. The corresponding (*h k l*) Miller

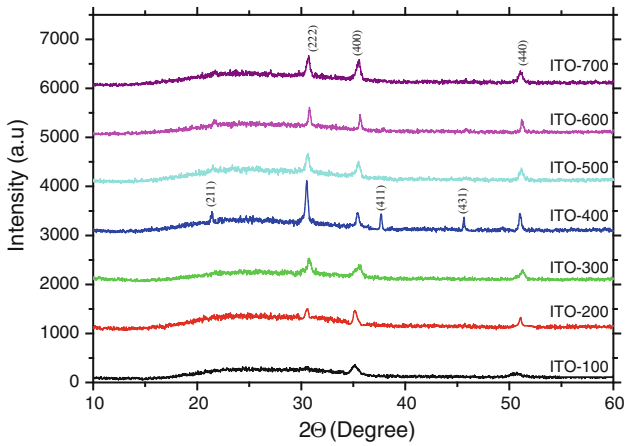

Fig. 1 XRD patterns of the ITO samples annealed at different temperature

indices belonging to the In_2O_3 main lines are shown in the diagrams. It is visible from the figure that all the samples produced contain the In_2O_3 phase only and exhibit the polycrystalline and cubic bixbite structure with more intensity of diffraction lines with increasing the annealing temperature up to 400 °C, illustrating that the tin atoms are probably doped substitutionally into the In_2O_3 lattice. Moreover, the film annealed at 100 °C does not displays a peak at $2\theta = 38.1°$ corresponding to (*411*) plane of In_2O_3. This phenomenon can be explained by the crystallization temperature (160–180 °C) of amorphous ITO films [34–36]. Figure 1 also shows that although the locations of the diffraction peaks do not change considerably, the peak intense dramatically increases with the enhancement in the substrate annealing temperature up to 400 °C. At the same time, some peak intensities such as (*222*), (*400*) and (*440*) enhance significantly with the increment in the annealing temperature while the peak (*211*) intensity starts to appear over the annealing temperature of 400 °C. Additionally, other peak intensities including (*411*) and (*431*) are observed only for the ITO-400 sample, confirming the coexistence of $\langle 411 \rangle$ and $\langle 431 \rangle$ textures. The peak (*222*) becomes very strong for this sample as a result of the preferred orientation in the direction of $\langle 111 \rangle$, attributed to the increment of the donor sites trapped at dislocations or point defects aggregates [37, 38]. Based on the XRD results, the different structure and orientation are observed for the samples produced in this research because of the fact that the structure and orientation of ITO films depend strongly on the energy of the sputtered particles arriving at the substrate. It was reported that [39–41], the thermalized atoms favor to crystallize in (*222*) orientation whereas the high energy particles prefer the (*400*) and (*440*) directions in consequence of their energy. The strongest intensity of (*222*) peak is obtained for the sample annealed at 400 °C, confirming that the ITO-400 has the best crystallinity and largest grain size among the other samples.

The ratio between the peak intensities of (*222*) and (*400*) is known as the crystal quality parameter. The I_{222}/I_{400} value is calculated for all the samples and the results obtained are listed in Table 1. It is apparent from the table that the parameter of the ITO-100 sample is about 0.85 (the smallest value among the values determined) which is much less than standard value of 3.33 ITO powder [42], meaning that the most part of layer parallel to the film surface is textured in $\langle 100 \rangle$ direction. On the other hand, the ratio of the ITO-400 sample is found to be near the standard value of the ITO powder (Table 1), showing that the layers of the ITO-400 sample obtain more oxygen vacancies compared to other ones, resulting in the (*222*) growth direction. Moreover, the lattice constant (*a*) and interplaner distances (*d*) calculated by means of the peak (*222*) for all the samples are tabulated in Table 1. As seen from the table, all the parameters obtained are found to be larger than the ITO standard parameters as a result of the growth induced stress [43], which stems from the oxygen deficiency [44, 45] and thermal expansion coefficient mismatch between the film and substrate [46, 47]. Additionally, the cell constants and interplaner distances of the samples produced in this work are found to decrease with the increase in the annealing temperature up to 400 °C beyond which these parameters are obtained to enhance slightly. Change of the parameters can be explained in terms of crystal growth in the (*400*) direction as a result of the stressed growth due to the variation of the oxygen vacancy number [48, 49].

Furthermore, the grain sizes of the samples prepared can be derived from the broadening nature of the XRD peaks following the Scherrer method [50–54]. The grain size *d* is given by

$$d = \frac{0.941\lambda}{B\cos\theta_B} \tag{1}$$

where *d* denotes the thickness of the crystal, λ is the wavelength, *B* presents the fullwidth half maximum (FWHM) of the Bragg peak corrected using the corresponding peak in micron-sized powder and θ_B is the Bragg angle. Further,

$$B^2 = B_m^2 - B_s^2 \tag{2}$$

where B_s is the half-width of the standard material in radians. The results obtained demonstrate that the grain sizes monotonously increase with the enhancement in the annealing temperature until 400 °C beyond which the crystallite size values start to slightly reduce. The largest grain size (54 nm) is obtained for the ITO-400 sample (Table 1) whereas the smallest one is found to be about 22 nm for ITO-100. According to the results, among the samples produced, the ITO-400 sample has the best crystallinity and connectivity between grains as a result of less number of grain boundaries, leading to less radiative

Table 1 X-ray intensity ratios, I_{222}/I_{400}, texture, grain size, lattice parameter and plane distance for the ITO films prepared at different annealing temperature

Main parameters	ITO-100	ITO-200	ITO-300	ITO-400	ITO-500	ITO-600	ITO-700
$\frac{I(222)}{I(400)}$	0.853	1.091	1.377	2.688	1.398	1.365	1.142
Texture	⟨100⟩	⟨100⟩	⟨100⟩	⟨111⟩	⟨111⟩	⟨100⟩	⟨100⟩
Lattice constant (Å)[a]	10.372	10.357	10.245	10.129	10.186	10.301	10.361
Plane distance (Å)[a]	2.992	2.874	2.958	2.924	2.941	2.963	2.984
Grain size from XRD (nm)	22	29	41	54	47	35	26

[a] The standard values for ITO powder are: cell constant (a_0) = 10.118 Å [40] and plane distance: (d_0) = 2.921 Å [39]

recombination centers or vise-versa [55, 56]. As well known, the improvement in the crystallinity is attributed to a decrease of donor sites trapped at the dislocations and grain boundaries, and also to the out-diffusion of oxygen atoms from interstitial positions [57].

3.2 Surface morphology

Atomic force microscopy (AFM) is useful method to both analyze the surface morphology of a thin film and obtain information about the thickness, roughness and height asymmetries values such as the skewness and kurtosis of the film [58, 59]. The typical AFM images corresponding to the ITO films annealed at 100 °C (the worst microstructure) and 400 °C (the best microstructure) are depicted in Fig. 2a and b, respectively. The surface scanned is 5 × 5 μm. It is visible from Fig. 2 that the surface morphology is strongly dependent upon the annealing temperature. The image of the ITO-100 sample illustrates smaller individual grains with higher roughness compared to that of the ITO-400 sample whereas a denser granular structure is observed for the latter, presenting the decrement in the separation between the grains. The grain size, average roughness and height asymmetry values are measured using the software analysis written by Nanomagnetic instrument and the results obtained are depicted in Table 2. It is apparent from the table that the crystallite size values are obtained to enhance with the increment in the annealing temperature up to 400 °C after which the values are observed to reduce from 64 to 39 nm monotonously. However, the smallest value of grain size is found to be about 32 nm for the ITO-100 sample. Further, the average crystallite sizes deduced from the AFM measurements are found to be greater than those inferred from the Scherrer method [60, 61]. Nevertheless, all the data obtained are observed to be in well agreement with each other (increase up to 400 °C of annealing temperature and then decrease).

Additionally, average roughness (S_a) and rms roughness parameter (S_q) are evaluated from the AFM images. As reported in literature, the former is the arithmetic mean or average of the absolute distances of the surface points from the mean plane whereas the latter is the root mean square of the surface departures from the mean plane within the sampling area [62]. S_a value can be calculated by the following relation:

$$S_a = \frac{1}{MN}\sum_{j=1}^{N}\sum_{i=1}^{M}|z|(x_i, y_j) \tag{3}$$

and S_q can be computed by means of the equation,

$$S_q \sqrt{\frac{1}{MN}\sum_{j=1}^{N}\sum_{i=1}^{M} z^2(x_i, y_j)} \tag{4}$$

where M denotes the number of columns in the surface and N is the number of rows in the surface. The S_a and S_q values obtained are given in Table 2. As seen from the table, the ITO-100 sample has the highest surface

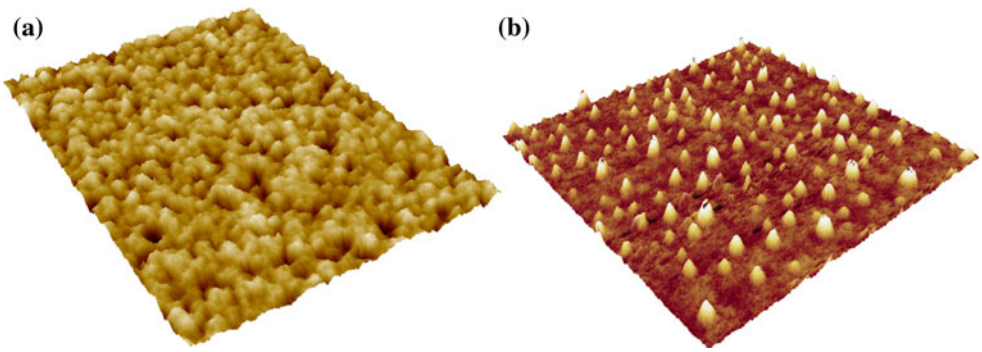

Fig. 2 Atomic force microscopy images of the ITO films annealed at **a** 100 °C and **b** 400 °C

Table 2 Microstructural, morphological and statistical parameters of the ITO films annealed at various temperature

Statistical parameters	ITO-100	ITO-200	ITO-300	ITO-400	ITO-500	ITO-600	ITO-700
Grain size from AFM (nm)	32	44	53	64	59	49	39
Average roughness (nm)	4.45	4.06	3.92	3.85	3.89	4.02	4.26
RMS roughness (nm)	4.58	4.13	4.04	3.96	4.01	4.09	4.38
Skewness, s_{sk}	1.04	1.06	1.09	1.10	1.10	1.07	1.05
Kurtosis, s_{ku}	1.11	1.17	1.26	1.31	1.29	1.22	1.16

roughness (S_a: 4.45 nm and S_q: 4.58 nm) among the films produced while the S_a of 3.85 and S_q of 3.96 are found to be the smallest values for the ITO-400 sample. Based on the results, the regular structures are observed on the surface of the films studied. However, the different surface roughness values might show the possible reason for the variation of the oxygen vacancies in the ITO films prepared. Moreover, similar results were reported in the literature [43, 63].

The height asymmetries including surface skewness and kurtosis are determined from the height distribution histogram for the samples [64]. The surface skewness (s_{sk}) is a measurement for the symmetry of the variation of a surface about its mean plane whereas the surface kurtosis (s_{ku}) is a measurement of the peakedness or sharpness of a surface. The former and latter of a sample can be computed from the following relations, respectively:

$$s_{sk} = \frac{1}{MNS_q^3}\sum_{j=1}^{N}\sum_{i=1}^{M} z^3(x_i, y_j) \tag{5}$$

$$s_{ku} = \frac{1}{MNS_q^4}\sum_{j=1}^{N}\sum_{i=1}^{M} z^4(x_i, y_j) \tag{6}$$

The s_{sk} and s_{ku} values calculated are tabulated in Table 2. One can see from the table that the surface skewness is obtained to be positive for all the samples while the surface kurtosis is found to be less than 3. According to the combination of the skewness and kurtosis values, all the film surfaces contain the disproportionate number of peaks and spread out distribution [59], confirming that the ITO thin films produced in this work can be useful for applications in technology and industry.

3.3 Transmittance spectra

It is argued that homogeneity, optical band gap energy, refraction index, porosity and photocatalytic performance of a semiconductor thin film can be determined with the aid of transmittance spectra [59]. As well known, high transmittance of a thin film indicates its low surface roughness, low refraction index, small crystallite size, high porosity and good homogeneity [65]. Figure 3 shows the transmittance spectra as a function of wavelength in the range of

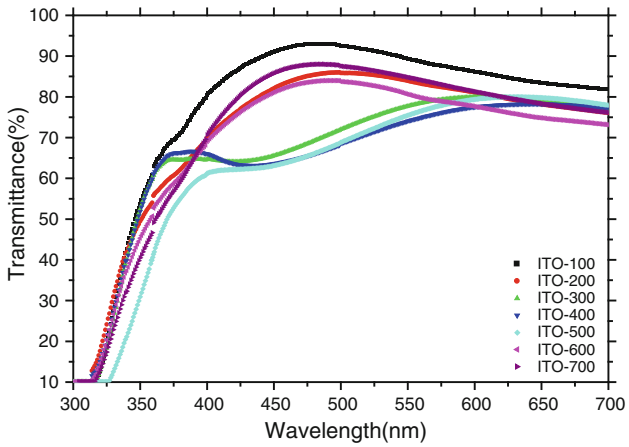

Fig. 3 Optical transmittance spectra of the ITO thin films

300–700 nm for the ITO thin films prepared in this work. As seen from the figure, no significant optical difference is observed for the transmittance curves, but the transmittance threshold shifts towards the lower energy as a result of the decrease in the optical band gap. The amplitude of interference oscillation of the thin films is obtained to be in a range of 78–93 %. The maximum transmittance is observed to be 78 % for the ITO-400 sample while the minimum transmittance is obtained to be 93 % for the ITO-100 film. A significant enhancement in the transmittance value is related to both the loss of light due to the oxygen vacancies and the growth of particles, supported by both XRD and AFM results. Based on these results, the ITO-400 sample obtains the largest crystallite and the best optical property among the ITO films studied; on the other hand, the ITO-100 film exhibits much better photoactivity than the other films.

3.3.1 Refractive index, packing density and porosity analyses

The refractive index (n_λ), a fundamental property of a thin film, is closely associated with the electronic polarizability of ions and local field inside the film [66]. Table 3 indicates the refractive index and porosity (evaluated from n_λ) values of the ITO films prepared at different annealing temperatures in a range of 100–700 °C. The former is

Table 3 Electro-optical characteristics of the ITO films with different annealing temperature

Electro-optical characteristics	ITO-100	ITO-200	ITO-300	ITO-400	ITO-500	ITO-600	ITO-700
Refraction index	1.72	1.77	1.85	1.94	1.89	1.81	1.75
Porosity (%)	45.57	37.45	28.96	18.96	24.57	33.25	39.52
Packing density	1.268	1.322	1.404	1.487	1.442	1.364	1.301
Optical band gap energy (eV)	3.92	3.85	3.76	3.68	3.72	3.81	3.89

derived from the optical transmittance data with the aid of the Swanepoel's envelope method [67], which is based on the analysis of the transmittance spectrum of a weakly absorbing film deposited on a non-absorbing substrate [68]. Hence, the refractive index (n_λ) over the spectral range is inferred from the envelopes fitted to the extrema measured:

$$n_\lambda = [N + (N^2 - n_0^2 n_1^2)^{1/2}]^{1/2} \tag{7}$$

$$N = 2n_0 n_1 \left[(T_{M(\lambda)} - T_{m(\lambda)})/T_{M(\lambda)} T_{m(\lambda)}\right] + (n_0^2 + n_1^2)/2 \tag{8}$$

where $T_{M(\lambda)}$ and $T_{m(\lambda)}$ are the transmittance maximum and minimum of the film at a wavelength ($\lambda = 500$ nm); n_0 denotes the refractive index of air ($n_0 = 1.00$) and n_1 presents the refractive index of the substrates (in our case $n_1 = 1.51$), respectively. The films prepared are considered as homogeneous structures in the computation. The calculated refractive indices of the ITO samples studied in this work are observed to be in the range from 1.72 to 1.94. Among the films studied, the ITO-400 (ITO-100) obtains the maximum (minimum) refractive index. However, the calculated refractive indices are found to be smaller than the values reported in [69] and [70] due to lesser packing density of grains and lower oxygen vacancies in the samples studied, meaning that the refractive index plays an important role on the determination of the packing density. In this study, the packing densities of the ITO samples are deduced from the following equation [71, 72],

$$n^2 = \frac{(1-p)n_v^4 + (1+p)n_v^2 n_s^2}{(1+p)n_v^2 + (1-p)n_s^2} \tag{9}$$

where n is the refractive index of the film studied, n_s denotes the substrate refractive index, n_v illustrates the void refractive index ($n_v = 1.00$ for air) and p is the packing density. For our samples, the packing density increases with ascending annealing temperature up to 400 °C after which the density starts to decrease monotonously (Table 3) as a result of the decrement in the refractive index of the samples. The maximum and minimum packing densities are obtained to be about 1,487 and 1.268 for the ITO-400 and ITO-100 sample, respectively.

Additionally, the porosity values of the ITO films are determined from the following equation [73]:

$$\text{Porosity} = \left(1 - \frac{n^2 - 1}{n_d^2 - 1}\right) \times 100(\%) \tag{10}$$

where the n_d is 2.1 (the refractive index of pore-free ITO) [21, 74] when the n denotes the refractive index of the porous thin film. The porosity values calculated are listed in Table 3. One can see from the table; like the XRD and AFM results, the porosity values reduce with the enhancement in the annealing temperature up to 400 °C after which the porosities start to increase again. The maximum porosity is found to be about 45.57 % for the ITO-100 sample while the porosity of 37.8 % is noted to be the minimum for the ITO-400 sample. Based on the results, the ITO-400 sample is least porous compared to the other films fabricated in this work, confirming that the refractive index, packing density and porosity of the ITO film studied are strongly dependent upon the annealing temperature.

3.3.2 Optical band gap energy analysis

As well known, there are several models and reports to find the optical absorption coefficient (α) and optical band gap energy (E_g) of a material [75]. In the present study, we assume a direct transition (value of the energy separation between the top of the valence band and the bottom of the conduction band) to determine the optical band gap energy of the samples studied [76]:

$$\alpha(h\upsilon) \propto A(h\upsilon - E_g)^2 \tag{11}$$

where α denotes absorption coefficient, A illustrates the edge width parameter and $h\upsilon$ is the photon energy. Figure 4 shows $(\alpha h\upsilon)^2$ versus photon energy (eV) plots for all the films prepared. The band gap values of the films are deduced from the extrapolation of the linear plots of $(\alpha h\upsilon)^{1/2}$ versus $h\upsilon$ when ($\alpha = 0$). The estimated values of optical band gap are obtained to be in a range of 3.68–3.92 eV. The ITO-100 sample has the maximum value of the E_g whereas the minimum value belongs to The ITO-400 sample. Based on these results, the energy band gap for the ITO-400 sample is obtained to shift to lower energy value, attributed to the increase in the grain size due to the quantum confinement effect [77–81]. As was reported in the previous studies [82, 83], the direct optical band gap of the ITO thin films changes from 3.5 to 4.5 eV. This wide

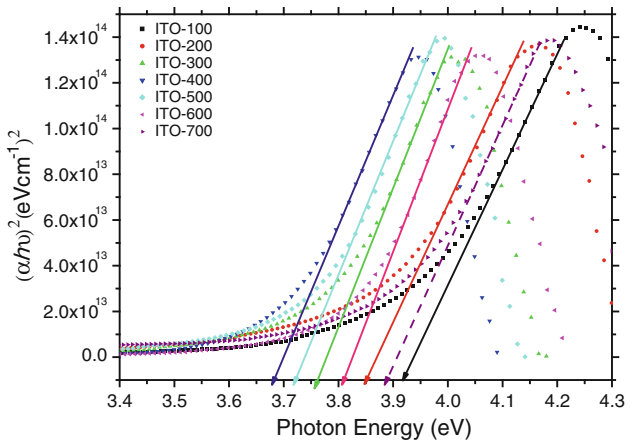

Fig. 4 Optical absorption coefficient α versus band gap energy (E_g) of the ITO films

range of the band gap for the degenerate semiconductor oxides such as TiO_2 and ITO is associated with two competing mechanisms: the first one is the band gap narrowing because of the electron–electron and electron-impurity effects on the valence and conduction bands, the second mechanism (Burstein–Moss effect) is the band gap widening due to the blocking of the lowest states of the conduction band by means of the excess electrons.

4 Conclusion

In this study, it is analyzed that how the annealing temperature affects the microstructural, optical and electrical properties of ITO thin films prepared on Soda lime glasses by the standard DC magnetron reactive sputtering technique. For the characterization of the samples produced, the XRD, AFM and UV–vis measurements are conducted. The results obtained indicate that the microstructural, optical and electrical properties of the films are found to depend strongly on the annealing temperature and the following findings are summarized:

- All the samples produced contain the In_2O_3 phase only and exhibit the polycrystalline and cubic bixbite structure with more intensity of diffraction lines with increasing the annealing temperature until 400 °C; however, the locations of the measured diffraction peaks do not change significantly. Moreover, some peak intensities including (*411*) and (*431*) are observed only for the ITO-400 sample, demonstrating the presence of ⟨*411*⟩ and ⟨*431*⟩ textures.
- The strongest intensity of (222) peak is obtained for the sample annealed at 400 °C, showing that the ITO-400 has the best crystallinity and largest grain size among the other samples as a result of the decrease in the donor sites trapped at the dislocations and grain boundaries, and the out-diffusion of oxygen atoms from interstitial positions. The smallest (greasiest) ratio I_{222}/I_{400} is also obtained for the ITO-100 (ITO-400) sample.
- The lattice constants and interplaner distances of the ITO thin films reduce with the enhancement in the annealing temperature up to 400 °C after which the parameters slightly increase due to the variation of the oxygen vacancy number causing the stressed growth.
- The maximum grain size of 54 nm is obtained for the ITO-400 sample as against 22 nm (minimum size) for the ITO-100 sample. Moreover, the ITO-400 sample has the best and densest granular structure owing to the reduction of the separation between the grains.
- The ITO-100 sample has the highest surface roughness (S_a: 4.45 nm and S_q: 4.58 nm) among the samples produced whereas the S_a of 3.85 and S_q of 3.96 are the smallest values for the ITO-400 sample.
- The surface skewness (s_{sk}) is obtained to be positive for all the samples while the surface kurtosis (s_{ku}) is found to be less than 3, meaning that all the film surfaces are found to be spread out distribution and comprised of disproportionate number of peaks.
- The transmittance of the ITO-400 film is found to be the smallest (78 %) while the ITO-100 sample is observed to have the maximum transmittance value (93 %) as a result of the different particle sizes. The refractive index of 1.94 is found to be the maximum for the former film.
- The ITO-100 is found to be most porous whereas the ITO-400 sample is noted to be densest among the films, supported by AFM images. Moreover, the former sample has the maximum band gap energy of 3.92 eV while the smallest optical band gap is obtained to be about 3.68 eV for the latter one.

References

1. J. Touskova, J. Kovanda, L. Dobiasova, V. Parizek, P. Kielar, Sol. Energ. Mat. Sol. C **37**, 65 (1995)
2. I. Hamberg, C.G. Granqvist, K.F. Berggren, B.E. Sernelius, L. Engstrom, Vacuum **35**, 9 (1985)
3. A. Romeo, M. Terheggen, D. Abou-Ras, D.L. Batzner, F.J. Haung, M. Kalin, D. Rudman, A.N. Tiwari, Prog. Photovolt. Res. Appl. **12**, 93 (2004)
4. H.M. Zeyada, M.M. El-Nahass, I.K. El-Zawawi, E.M. El-Menyawy, Eur. Phys. J. Appl. Phys. **49**, 10301 (2010)
5. S.K. Poznyak, A.N. Golubev, A.I. Kulak, Surf. Sci. **454**, 396 (2000)
6. D.G. Parker, P.G. Say, Electron. Lett. **22**, 7 (1986)
7. M.C. de Andrade, S. Moehlecke, Appl. Phys. A **58**, 6 (1994)
8. K.L. Chopra, P.D. Paulson, V. Dutta, Prog. Photovolt. Res. Appl. **12**, 69 (2004)

9. R. Tueta, M. Braguier, Thin Solid Films **80**, 8 (1981)
10. T.J. Coutts, X. Li, M.W. Wanlass, K.A. Emery, T.A. Cessert, IEEE Electron Device Lett. **26**, 660 (1990)
11. M. Masuda, K. Sakuma, E. Satoh, Y. Yamasaki, H. Miyasaka, J. Takeuchi, in *Proc. 6th Int. Electron. Manuf. Technol. Symp.*(1989), p. 95
12. E. Takeda, T. Kawaguchi, Y. Nanno, H. Tsutsu, T. Tamura, S. Ishihara, S. Nagata, in *Proc. Int. Display Research Conf.* (1988), p. 155
13. P.P. Deimel, B.B. Heimhofer, G. Krotz, H.J. Lilienhof, J. Wind, G. Muller, E. Voges, IEEE Photon Technol. Lett. **2**, 449 (1990)
14. Y.S. Kim, Y.C. Park, S.G. Ansari, J.Y. Lee, B.S. Lee, H.S. Shin, Surf. Coat. Technol. **173**, 299 (2003)
15. M.S. Hwang, H.J. Lee, H.S. Jeong, Y.W. Seo, S.J. Kwon, Surf. Coat. Technol. **171**, 29 (2002)
16. S.H. Keshmiri, M. Rezaee-Roknabadi, S. Ashok, Thin Solid Films **413**, 167 (2002)
17. S. Ishibashi, Y. Higuchi, Y. Ota, K. Nakamura, J. Vac. Sci. Technol. **A 8**, 1403 (1990)
18. I. Hamberg, C.G. Grangvist, J. Appl. Phys. **60**, R123 (1986)
19. A. Antony, M. Nisha, R. Manoj, M.K. Jayaraj, Appl. Surf. Sci. **225**, 294 (2004)
20. V. Senthilkumara, P. Vickramana, M. Jayachandran, C. Sanjeevirajac, Vacuum **84**, 864 (2010)
21. H.Y. Yeom, N. Popovich, E. Chason, D.C. Paine, Thin Solid Films **411**, 17 (2002)
22. H. Morikawa, M. Fujita, Thin Solid Films **359**, 61 (2000)
23. M.J. Alam, D.C. Cameron, Thin Solid Films **420–421**, 76 (2002)
24. Y.S. Jung, Solid State Commun. **129**, 491 (2004)
25. F. Zhu, C.H.A. Huan, K.Z. Hang, A.T.S. Wee, Thin Solid Films **359**, 244 (2000)
26. Y. Nishio, T. Sei, T. Tsuchiya, J. Mater. Sci. **31**, 1761 (1996)
27. H.S. Kwok, X.W. Sun, D.H. Kim, Thin Solid Films **335**, 299 (1998)
28. H. Kim, A. Pique, J.S. Horwitz, Appl. Phys. Lett. **74**, 344 (1999)
29. R.B.H. Tahar, T. Ban, Y. Ohya, Y. Takahashi, J. Appl. Phys. **83**, 2139 (1998)
30. G. Yildirim, S. Bal, and A. Varilci, J. Supercond. Nov. Magn. (2012). doi:10.1007/s10948-012-1497-1
31. L. Tsarkova, A. Knoll, G. Krausch, R. Magerle, Macromolecules **39**, 3608 (2006)
32. I. Zalakain, J.A. Ramos, R. Fernandez, H. Etxeberria, I. Mondragon, J. Appl. Polym. Sci. **25**, 1552 (2012)
33. W.V. Zoelen, E. Polushkin, G.T. Brinke, Macromolecules **41**, 8807 (2008)
34. J.H. Lee, J. Electroceram. **23**, 554 (2009)
35. C.W. Ow-Yang, D. Spinner, Y. Shigesato, D.C. Paine, J. Appl. Phys. **83**, 45 (1998)
36. P.K. Song, H. Akao, M. Kamei, Y. Shigesato, I.Y. Asui, Jpn. J. Appl. Phys. **38**, 5224 (1999)
37. N. Manavizadeh, A. Khodayari, E. Asl Soleimani, S. Bagherzadeh, Iran. J. Chem. Chem. Eng. **28**, 57 (2009)
38. Y. Shigesato, D.C. Paine, Thin Solid Films **238**, 44 (1994)
39. E. Terzini, G. Nobile, S. Loreti, C. Minarini, T. Polichetti, P. Thilakan, Jpn. J. Appl. Phys. **38**, 3448 (1999)
40. A. Mohammadi Gheidari, F. Behafarid, G. Kavei, M. Kazemzad, Mater. Sci. Eng. **B 136**, 37 (2007)
41. C.V.R. Vassant Kumar, A. Mansingh, J. Appl. Phys. **65**, 1270 (1989)
42. C. Guillen, J. Herrero, Thin Solid Films **510**, 260 (2006)
43. L. Kerkach, A. Layadi, E. Dogheche, D. Remiens, J. Phys. D Appl. Phys. **39**, 184 (2006)
44. J. Ye, K. Nakamura, Phys. Rev. B **48**, 7554 (1993)
45. S. Shin, Mater. Res. Bull. **16**, 299 (1981)
46. W.F. Wu, B.S. Chiou, Thin Solid Films **293**, 244 (1997)
47. E. Fortunato, I. Ferreira, F. Giuliani, P. Wurmsdobler, R. Martins, J. Non-Cryst, Solids **1213**, 266 (2000)
48. P. Thilakan, C. Minarini, S. Loreti, E. Terzini, Thin Solid Films **388**, 34 (2001)
49. D. Kim, Y. Han, J. S. Cho, S. K. Koh, Thin Solid Films **377/378**, 81 (2000)
50. G. Yildirim, A. Varilci, M. Akdogan, C. Terzioglu, J. Mater. Sci Mater. Electron. (2011). doi:10.1007/s10854-011-0522-7
51. J. Economy, R. Anderson, Inorg. Chem. **5**, 989 (1966)
52. S. Bal, M. Dogruer, G. Yildirim, A. Varilci, C. Terzioglu, Y. Zalaoglu, J. Supercond. Nov. Magn. (2011). doi:10.1007/s10948-011-1360-9
53. B.D. Cullity, *Element of X-ray Diffraction*, 3rd edn. (Addition-Wesley, Reading MA, 2001)
54. G. Yildirim, S. Bal, E. Yucel, M. Dogruer, M. Akdogan, A. Varilci, C. Terzioglu, J. Supercond. Nov. Magn. (2011). doi:10.1007/s10948-011-1324-0
55. G. Jayalakshmi, N. Gopalakrishnan, B.K. Panigrahi, T. Balasubramanian, Crst. Res. Technol. **12**, 1257 (2011)
56. B.L. Zhu, X.Z. Zhao, S. Xu, F.H. Su, G.H. Li, X.G. Wu, J. Wu, R. Wu, J. Liu, Jpn. J. Appl. Phys. **47**, 2225 (2008)
57. Gokcen M, Bal S, Yildirim G, Gulen M, Varilci A, J. Mater. Sci. Mater. Electron. (2012). doi:10.1007/s10854-012-0690-0
58. G. Yildirim, S. Bal, M. Gulen, A. Varilci, E. Budak, M. Akdogan, Cryst. Res. Technol. **47**, 195 (2012)
59. G. Yildirim, M. Akdogan, A. Varilci, C. Terzioglu, Cryst. Res. Technol. **45**, 1161 (2010)
60. H. Kim, J.S. Horwitz, G. Kushto, A. Pique, Z.H. Kafafi, C.M. Gilmore, D.B. Chrisey, J. Appl. Phys. **88**, 6021 (2000)
61. G. Korotcenkov, V. Brinzari, A. Cerneavschi, M. Ivanov, V. Golonvanov, A. Cornet, J. Morante, A. Cabot, J. Arbiol, Thin Solid Films **406**, 315 (2004)
62. I.V. Tudose, P. Horvath, M. Suchea, S. Christoulakis, T. Kitsopoulos, G. Kiriakidis, J. Appl. Phys. **89**, 57 (2007)
63. H. Kim, C.M. Gilmore, J. Appl. Phys. **86**, 6451 (1999)
64. C.S. Yadav, P.L. Paulose, New J. Phys. **11**, 103046 (2009)
65. R. Thomas, D.C. Dube, M.N. Kamalasanan, S. Chandra, Thin Solid Films **346**, 212 (1999)
66. M.M. El-Nahass, E.M. El-Menyawy, Mater. Sci. Eng. B Adv. **177**, 145 (2012)
67. R. Swanepoel, J. Phys. E Sci. Instrum. **16**, 1214 (1983)
68. J.C. Manifacier, J. Gasiot, J.P. Fillard, J. Phys. E **9**, 1002 (1976)
69. W.W. Mobzen, J. Vac. Sci. Technol. **12**, 99 (1975)
70. J. Szczyrbowski, A. Dietrich, H. Hoffmann, Phys. Stat. Sol. A **78**, 243 (1983)
71. H.A. Macleod, J. Vac. Sci. Technol. **A 4**, 418 (1986)
72. W.L. Bragg, A.B. Pippard, Acta Crystallogr. **6**, 865 (1953)
73. B.E. Yoldas, P.W. Partlow, Thin Solid Films **129**, 1 (1985)
74. S.A. Kinckerbocker, A.K. Kulkarni, J. Vac. Sci. Technol. **A 143**, 757 (1996)
75. H.N. Cui, V. Teixeira, A. Monteiro, Vacuum **67**, 589 (2002)
76. J.I. Pankove, *Optical Processes in Semiconductors*, 2nd edn. (Dover Publications Inc., New York, 1970)
77. Y.D. Glinka, S.H. Lin, L.P. Hwang, Y.T. Chen, N.H. Tolk, Phys. Rev. B **64**, 085421 (2001)
78. G.L. Tian, H.B. He, J.D. Shao, Chin. Phys. Lett. **22**, 1787 (2005)
79. F.M. Liu, T.M. Wang, J.Q. Li, C. Wang, S.K. Zheng, M. Duan, J. Magn. Magn. Mater. **251**, 245 (2002)
80. Y.K. Chang, H.H. Hsieh, W.F. Pong, M.H. Tsai, F.Z. Chien, P.K. Tseng, L.C. Chen, T.Y. Wang, K.H. Chen, D.M. Bhusari, J.R. Yang, S.T. Lin, Phys. Rev. Lett. **82**, 5377 (1999)
81. J.T. Jiu, F.M. Wang, M. Adachi, Mater. Lett. **58**, 3915 (2004)
82. J.F. Smith, A.J. Aronson, D. Chen, W.H. Class, Thin Solid Films **72**, 469 (1980)
83. M.J. Alam, D.C. Cameron, Thin Solid Films **377–378**, 455 (2000)